Cobalt Molybdenum Nitride-Based Nanosheets for Seawater Splitting

Xiang Wang,[a,b] Xu Han,[c] Ruifeng Du,[a,b] Congcong Xing,[a,d] Xueqiang Qi,[e] Zhifu Liang,[a,c] Pablo Guardia,[a] Jordi Arbiol,[c,f] Andreu Cabot,*[a,f] Junshan Li*[g]

a Catalonia Institute for Energy Research (IREC), Sant Adrià de Besòs, 08930 Barcelona, Spain

b Departament d'Enginyeria Electrònica i Biomèdica, Universitat de Barcelona, 08028, Barcelona, Catalonia, Spain

c Catalan Institute of Nanoscience and Nanotechnology (ICN2), CSIC and BIST, Campus UAB, Bellaterra, 08193 Barcelona, Catalonia, Spain

d Institute of Energy Technologies, Department of Chemical Engineering and Barcelona Research Center in Multiscale Science and Engineering, Universitat Politècnica de Catalunya, EEBE, 08019, Barcelona, Catalonia, Spain

e College of Chemistry and Chemical Engineering, Chongqing University, Chongqing 400044, China.

f ICREA Pg. Lluis Companys, 08010 Barcelona, Catalonia, Spain

g Institute of Advanced Study, Chengdu University, Chengdu 610106, China

* E-mails: A. Cabot: acabot@irec.cat; J. Li: lijunshan@cdu.edu.cn.

Abstract

The development of cost-effective bifunctional catalysts for water electrolysis is both a crucial necessity and an exciting scientific challenge. Herein a simple approach based on a MOF sacrificial template to preparing cobalt molybdenum nitride supported on nitrogen-doped carbon nanosheets is reported. The porous structure of produced composite enables fast reaction kinetics, enhanced stability and high corrosion resistance in critical seawater conditions. The cobalt molybdenum nitride-based electrocatalyst is tested toward both OER and HER half-reactions using seawater electrolyte, providing excellent performances that are rationalized using density functional theory (DFT). Subsequently, the nitride composite is tested as a bifunctional catalyst for the overall splitting of KOH-treated seawater from the Mediterranean Sea. The assembled system requires overpotentials of just 1.70 V to achieve a current density of 100 mA cm^{-2} in 1 M KOH seawater and continuously works for over 62 h. This work demonstrates the potential of transition metal nitrides for seawater splitting and represents a step forward toward the cost-effective implementation of this technology.

Keywords: Molybdenum nitride, Cobalt nitride, Electrocatalysis, Seawater splitting, Hydrogen

1. Introduction

Seawater is an abundant natural resource, accounting for over 96% of the planet's total water and presenting a fairly homogeneous geographical distribution.[1,2] Thus its use as an alternative feedstock to produce hydrogen, replacing fossil fuels, is extremely appealing.[3-8] However, implementing cost-effective seawater splitting systems remains a major challenge. The first main limitation of the use of seawater to generate hydrogen is its high salt concentration (about 3.5 wt%) and the kinetically unfavourable water oxidation to O_2 (oxygen evolution reaction, OER, $4OH^- \rightarrow O_2$ + $2H_2O + 4e^-$) over the chloride oxidation to chlorine (chlorine evolution reaction, CER, $2Cl^- \rightarrow Cl_2$ + $2e^-$).[9-11] Besides, in alkaline media, at an onset potential of about 490 mV, Cl_2 further reacts with OH^- to form hypochlorite, which is toxic and highly corrosive. Thus, high-performance OER catalysts with high OER activities at overpotentials well below 490 mV are required to avoid the formation of hypochlorite.[12-14] Additional challenges in the electrochemical seawater splitting are the medium/long-term corrosion by chloride and the existence of ions, suspended particles, bacteria and other microbes that can poison the electrocatalyst reducing its performance.[10, 13, 15, 16, 35] Therefore, electrocatalysts with proper micro and macrostructures that facilitate the water diffusion without being blocked are desirable.

Among possible candidates, transition-metal nitrides (TMNs) are particularly interesting electrocatalysts for seawater splitting owing to their unique d-band electron configurations, intrinsic metallic characteristics providing high electrical conductivities, good corrosion resistance and strong mechanical properties.[17, 18] Besides, the metal–nitrogen bond endows the metal nitrides with an electron-donating character that promotes proton adsorption.[19, 20] All these properties contribute to the higher catalytic activity of the TMN compared with the corresponding transition metal. Besides, the engineering of multimetallic nitrides and composites allows further tailoring of the d-band position to modulate the adsorption ability of electrocatalysts and to achieve optimized catalytic performance.[21, 22] Nevertheless, while significant efforts have been invested into producing efficient TMN electrocatalysts for pure water electrolysis, the performance of these catalysts in seawater conditions has been rarely investigated.

Here we detail the synthesis of thin cobalt molybdenum nitride particles, that we denote as MoN-Co_2N, supported by nitrogen-doped carbon nanosheets (NSs) as an effective seawater

electrocatalyst. The nitride composite is obtained from a ZIF-67 metal-organic framework (MOF) as a self-sacrificial template, taking advantage of its open crystalline structure, high surface area, well-defined pores, tunable functionality and rich carbon content.[23, 24] The NS morphology is selected to shorten charge and mass transfer distance, accelerating the diffusion of reactants, and to maximize the percentage of surface unsaturated atoms, the exposition of active sites and thus the electroactive surface area.[7, 25-27] This catalyst is tested toward both OER and HER using a 1 M KOH-treated seawater electrolyte. Owing to its high performance in both half-reactions, MoN-Co$_x$N is used as a bifunctional catalyst for the overall splitting of natural seawater obtained from the Mediterranean Sea and incorporating 1 M KOH. The obtained performances are compared with the benchmark IrO$_2$ ‖ Pt/C pair. The excellent results obtained are rationalized using density functional theory (DFT) calculations.

2. Results and discussion

2.1. Characterization of electrocatalysts

Cobalt molybdenum nitride supported on nitrogen-doped carbon NSs were produced in three steps, as depicted in Figure 1. First, a cobalt-based zeolitic imidazolate framework (ZIF-67) was prepared as a 3D template with high carbon content and suitable porous nanostructure.[28, 29] Figure 2a displays a representative SEM micrograph of the ZIF-67 template particles, which were characterized by a rhombic dodecahedron geometry with an average size of 500 nm.
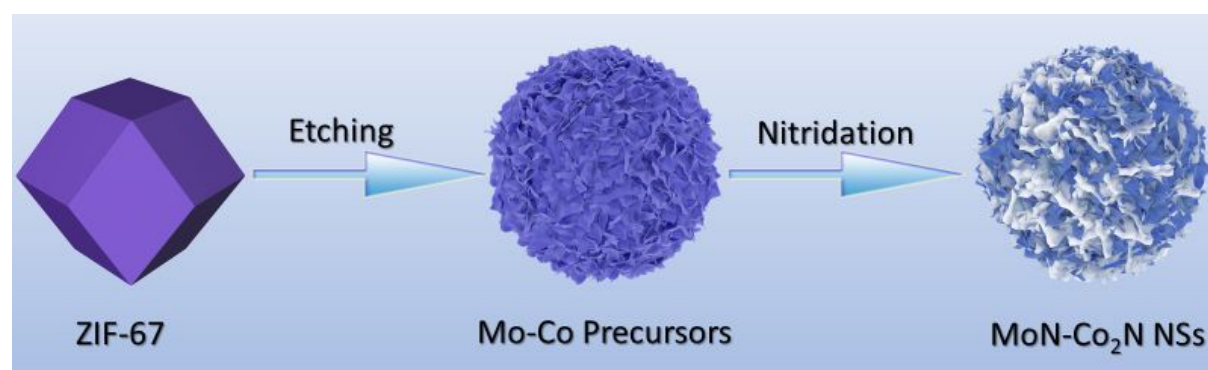

Figure 1. Schematic illustration of the synthesis of MoN-Co$_2$N nanosheets.

In a second step, the ZIF-67 was etched and Co was partially exchanged with Mo using ammonium molybdate both as Mo source and etching agent. In this step, ammonium molybdate hydrolyzes generating protons (H$^+$) that slowly etch the ZIF-67 releasing Co^{2+} ions, and hydroxides (OH$^-$) that

drive the precipitation of 2-methylimidazole and molybdate and cobalt ions.[30, 31] Thus, upon hydrolysis and etching processes with ammonium molybdate, the crystalline ZIF-67 dodecahedron particles were transformed into an amorphous and layered material, as observed in Figures 2b and S1.

Finally, the amorphous Mo-Co precursor sample was annealed at 500 °C for 2 h under NH_3/Ar atmosphere. In this nitridation step, the Mo-Co precursor transformed into a nitrogen-doped composite that conserved an ultrathin nanosheet structure (Figures 2c and S2). EDS analysis of the annealed material revealed an overall Co:Mo molar ratio of Co/Mo = 3.2 (Figure S3). TEM images (Figures 2d,g, S4, and S5) further confirmed the 2D ultrathin NS morphology of the annealed material and revealed the presence of numerous holes on the NSs. Such pores can be formed by the H_2O loss from the Mo-Co precursor during the nitridation process. We foresee these holes as highly convenient to promote the transport of electrolyte and overall improve the catalytic activity.[32] Unlike the Mo-Co precursor, the annealed samples displayed no less than two interconnected phases, a nitrogen-doped carbon and at least a Mo-Co-N phase (Figures 2 g, S4, and S5). The ultrathin carbon-based layer originated from the ligand decomposition in the presence of ammonia (Figure 2d) and can contribute to the charge transport within the electrodes.[33, 34] Lying flat on this carbon support, a uniform loading of Mo-Co-N NS-like particles was observed (Figures 2g). HRTEM characterization of the Mo-Co-N particles revealed the presence of at least two phases, MoN and Co_2N (Figures 2e,f and S6). Figure 2e displays an HRTEM image of a crystal structure that matches well with the Co_2N orthorhombic phase (space group =Pmnn) with a=2.8535 Å, b=4.6056 Å, c=4.3443 Å. Figure 2f displays an HRTEM image of a crystallographic domain matching the MoN trigonal phase (space group =P-31m) with a=b=5.6650 Å, and c=5.5200 Å. While different phases were identified by HRTEM analysis, STEM-EELS elemental maps displayed a uniform distribution of N, Co and Mo throughout the entire Mo-Co-N particles (Figures 2h and S7). Thus, we hypothesize that both phases, MoN and Co_2N, are intimately interconnected within MoN-Co_2N heterostructures. Figure 3a shows an AFM image of the MoN-Co_2N NSs, which allowed to determine the NS thickness to be ca. 3.2 nm (Figure 3b).
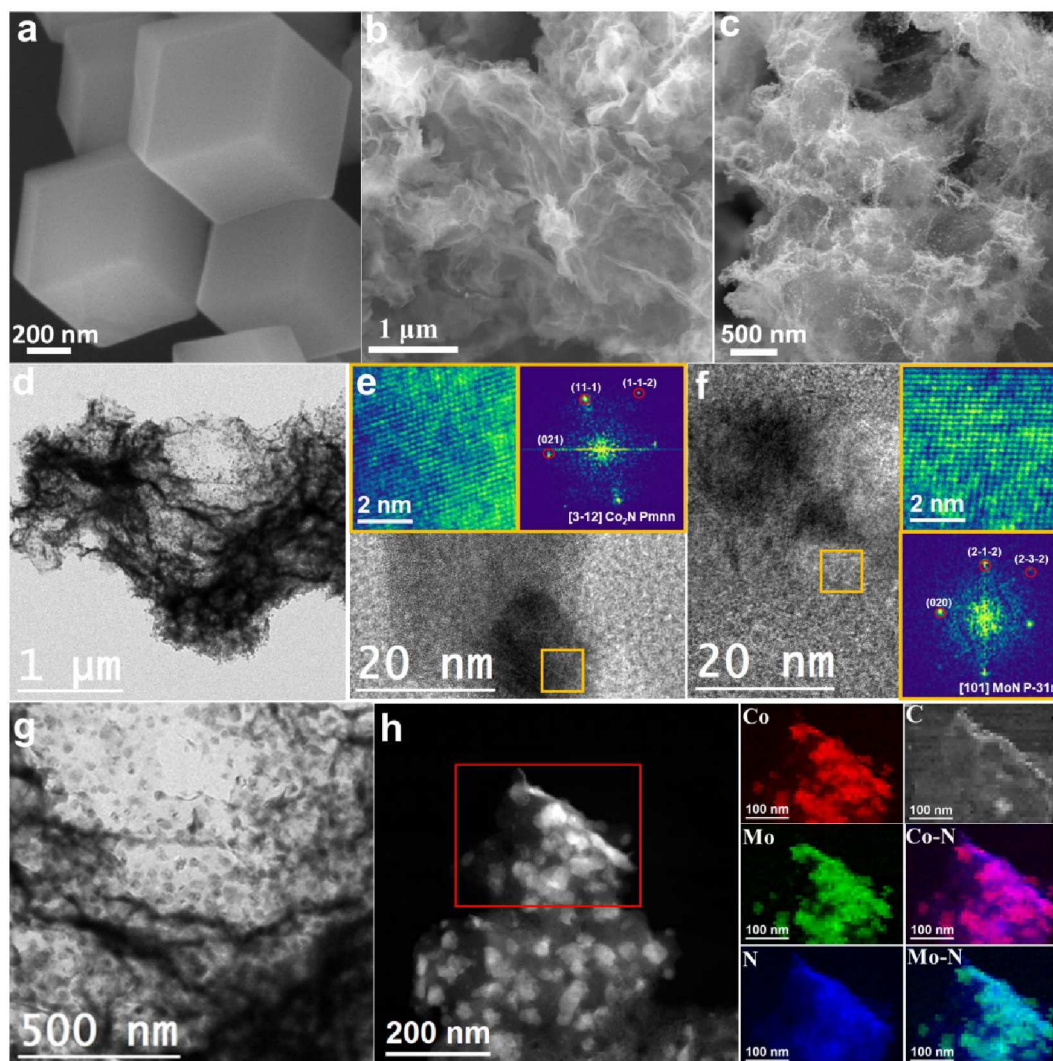
Figure 2. a-c) SEM images of ZIF-67 (a), Mo-Co precursor (b), and MoN-Co$_2$N (c). d, g) TEM image of MoN-Co$_2$N. e) HRTEM image of the MoN-Co$_2$N structure, magnified detail of the orange squared region and its corresponding indexed power spectrum, showing that this crystal corresponds to the orthorhombic Co$_2$N phase, visualized along its [3-12] zone axis. f) HRTEM image of the MoN-Co$_2$N structure, magnified detail of the orange squared region and its corresponding power spectrum, showing that the selected crystal corresponds to the trigonal MoN phase, visualized along its [101] zone axis. h) STEM image of MoN-Co$_2$N NSs and EELS chemical composition maps obtained from the red squared area of the STEM micrograph. Individual Co L$_{2,3}$-edges at 779 eV (red), Mo M$_{4,5}$-edges at 227 eV (green), N K-edge at 401 eV (blue) and C K-edge at 284 eV (grey) and composites of Co-N and Mo-N.

XRD analysis showed ZIF-67 to be highly crystalline (Figure 3d). In contrast, XRD patterns showed the Mo-Co precursor to be amorphous (Figure 3d) but to recover a crystallographic order after the nitridation step (Figure 3e). As shown in Figure S8, the XRD peaks obtained from the MoN-Co$_2$N sample at 32.7° and 44.3° can be assigned to MoN and Co$_2$N phases, respectively, which would be

5

consistent with HRTEM results. Raman spectroscopy was used to further analyze the structural properties of the material. The Raman spectrum of MoN-Co$_2$N NSs showed four Raman bands, at about 482, 512, 619 and 682 cm^{-1}, that are assigned to the E$_g$, F$_{2g}$, and A$_{1g}$ vibration modes of Co$_2$N, respectively (Figure 3f). [38, 39] Besides, a band at 930 cm^{-1} is associated with the MoN phase.[40] These bands are slightly shifted compared with literature values, which demonstrates the interaction between MoN and Co$_2$N crystal lattices.

To study the Mo precursor effect on the morphology of the final product, we replaced the ammonium molybdate with sodium molybdate. The product obtained after the Mo introduction was denoted as Na$_2$MoO$_4$-ZIF-67. XRD analysis showed Na$_2$MoO$_4$-ZIF-67 to display a similar crystal structure as ZIF-67 (Figure 3d). After the nitridation step, the material obtained with an ammonium-free Mo precursor displayed a much more compact nanocage-like morphology (Figure S9). Besides, EDS analysis of this sample, denoted as Mo-Co$_2$N, revealed a low molybdenum content (Co/Mo = 8.6). As a reference, a Mo-free Co$_x$N was obtained by annealing the ZIF-67 in the ammonia atmosphere, with no etching step (Figure S10). The obtained material, Co$_x$N, also displayed a more compact morphology than the MoN-Co$_2$N NSs. XRD patterns showed the Co$_x$N sample to display intense peaks at about 44° and 51° that could be potentially assigned to Co, Co$_4$N or other Co$_x$N phases (Figures 3e and S8). Taking into account the effectiveness of the nitration process observed from the large amount of nitrogen observed by EELS, EDX and XPS (below), we discarded the presence of metallic Co. Besides, the Raman spectrum of Co$_x$N showed the vibration bands, at about 480, 510, 620, and 680 cm^{-1} assigned to the E$_g$, F$_{2g}$, and A$_{1g}$ vibration modes of Co$_x$N, respectively (Figure 3f), further discarding the assignment of the XRD pattern to Co. [38, 39]

The surface area and porosity of the prepared catalysts were analysed from nitrogen adsorption-desorption isotherms. As shown in Figure 3c, MoN-Co$_2$N exhibits a type-IV isotherm with an H3-type hysteresis loop at high relative pressures (0.8–1.0 P/P$_0$). The Brunauer–Emmett–Teller (BET) specific surface area of MoN-Co$_2$N was 228 m^2 g^{-1}, well above that of Co$_x$N (44.5 m^2 g^{-1}). The average pore size and the cumulative pore volume of MoN-Co$_2$N were 15.8 nm and 0.53 cm^3 g^{-1}, respectively (Figure S11). This result revealed the existence of a large density of mesopores within the material, related to the holey NS structure, which is highly positive to increasing electroactive surface area and the rate of transport of reactants, including hydrion/ hydroxide ions, and products, such as oxygen and hydrogen.[36, 37]

6

As shown in Figure 3g, the N 1s XPS spectrum displays three peaks at 399.3, 395.1, and 397.3 eV, corresponding to pyridinic N, M-N and pyrrolic N, respectively.[41] The whole N 1S spectrum shifts towards lower binding energies with the incorporation of Mo, denoting a partial electron transfer from the transition metals towards the N. In the Co 2p spectra (Fig. 4h), two 2p doublets and the corresponding satellite peaks were identified. The two doublets, at Co $2p_{3/2}$ 782.1 eV and 780.3 eV were assigned to $Co^{2+/3+}$ ions within two different chemical environments that we associated with the Co_2N lattice and a surface oxidized component.[42, 43] The Mo 3d XPS spectrum also displayed two doublets (Figure 4i), the doublet located at 229.8 eV (Mo $3d_{5/2}$) was associated with Mo^{4+}, and the doublet located at 232.1 eV (Mo $3d_{5/2}$) with Mo^{6+}.[44, 45]
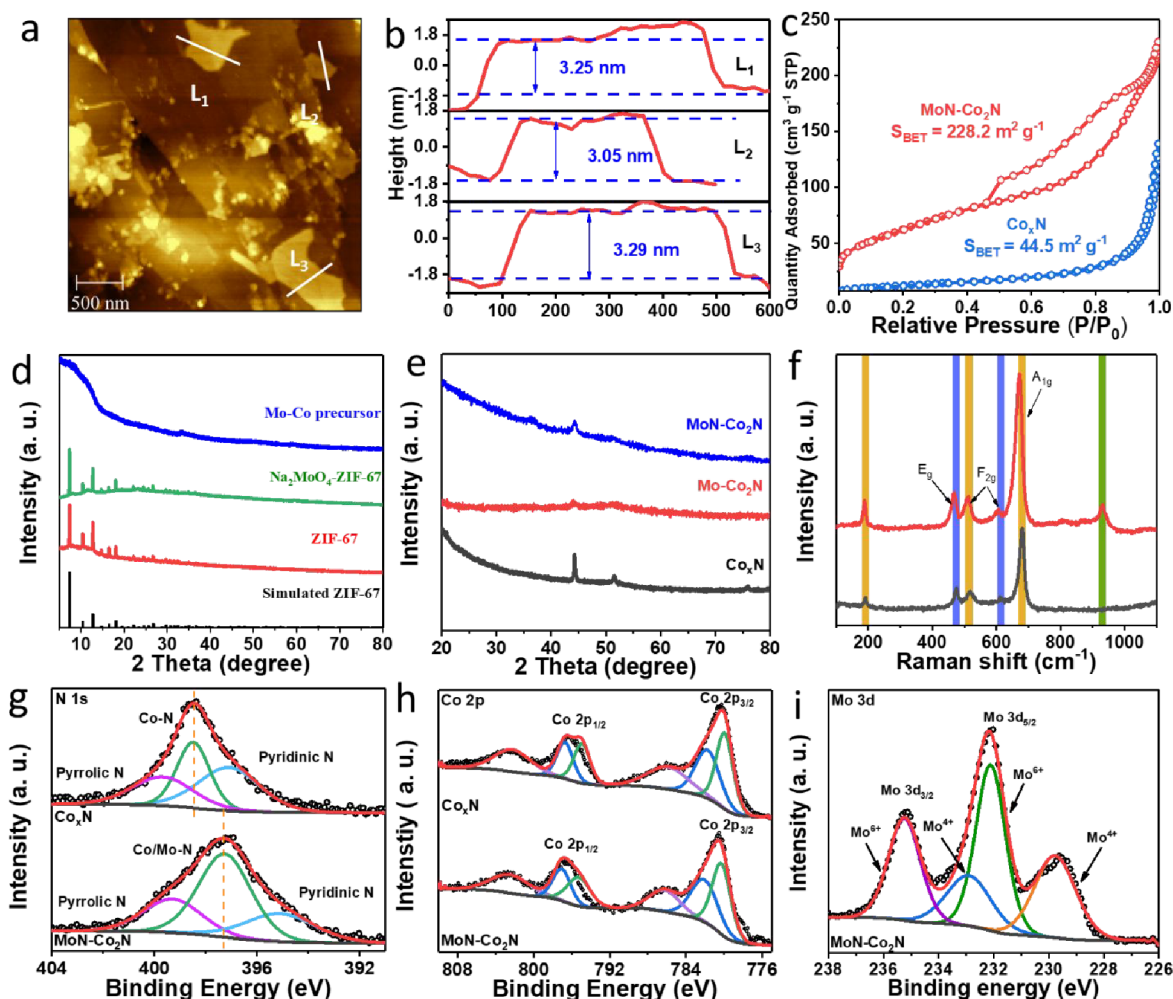

Figure 3. a) AFM image of MoN-Co$_2$N NSs. b) AFM line profiles for a few MoN-Co$_2$N NSs as displayed in panel a. c) N$_2$ adsorption-desorption isotherms for MoN-Co$_2$N and Co$_x$N. (d,e) XRD pattern of d) different precursors, e) MoN-Co$_2$N, Mo-Co$_2$N and Co$_x$N. f) Raman spectra for MoN-Co$_2$N (red) and Co$_x$N (black). High-resolution XPS spectra of g) N 1s, h) Co 2p, i) Mo 3d for MoN-Co$_2$N.

2.2. Oxygen evolution reaction

The electrocatalytic performance of Co_xN-, Mo-Co_2N- and MoN-Co_2N-based catalysts was evaluated using a three-electrode configuration. As additional references, commercial IrO_2 and Pt/C catalysts were also tested for OER and HER reactions, respectively.

Figure 4a,b displays the OER LSV curves obtained in a 1 M KOH electrolyte. LSV curves revealed the MoN-Co_2N electrocatalyst to be characterized by the highest OER catalytic activities. MoN-Co_2N electrocatalyst required an overpotential of 267 mV to achieve 10 mA cm^{-2} of current density and 309 mV to drive 100 mA cm^{-2}. These overpotentials are significantly lower than those measured from IrO_2 (323 and 428 mV), Mo-Co_2N (288 and 375 mV), and Co_xN (321 mV and 421). As displayed in Figure 4c, the Tafel slope of MoN-Co_2N was just 35.6 mV dec^{-1}, well below that of Mo-Co_2N (58.3 mV dec^{-1}) and Co_xN (65.7 dec^{-1}). The small Tafel slopes obtained with the MoN-Co_2N catalysts demonstrate fast OER electrocatalytic kinetics. Overall, the MoN-Co_2N OER performance was significantly improved over most other TMN electrocatalysts reported to date (Figure 4d, Table S1).

Figure 4e displays the double-layer capacitances (C_{dl}) measured from CV data (Figure S12) for the different catalysts, as an indication of their electrochemically active surface area (ECSA).[34] The MoN-Co_2N catalyst exhibited the largest C_{dl} (15.01 mF cm^{-2}) among the tested catalysts, well above that of Mo-Co_2N (10.35 mF cm^{-2}), almost threefold higher than that of Co_xN (5.07 mF cm^{-2}) and over tenfold higher than IrO_2 (1.27 mF cm^{-2}). The related MoN-Co_2N ECSA was as high as 375.25 cm^{-2} (Table S2). Nevertheless, even when normalizing the OER current density to the ECSA, the MoN-Co_2N electrocatalyst still displayed the highest OER activity values (Figure 4f).

The electron transport and transfer properties of the electrocatalysts were evaluated by EIS (Figure 3g). The MoN-Co_2N catalyst exhibited the lowest charge-transfer resistance (R_{ct} = 28.0 Ω), significantly below that of Mo-Co_2N (54.6 Ω), Co_xN (82.8 Ω) and IrO_2 (11.7 Ω), confirming its fast charge transfer rate.

The OER durability of the MoN-Co_2N electrocatalyst was evaluated in a 1 M KOH electrolyte by analyzing the variation of the LSV curve after 3,000 CV cycles. As observed in Figure 4h, the initial and final LSV curves almost overlapped, which confirms the excellent cycling stability of the MoN-Co_2N electrocatalyst. Besides, a chronoamperometry measurement of the MoN-Co_2N catalyst in alkaline conditions showed a negligible current density decay after 100 h of continuous OER operation at 267 mV (Figure 4i).
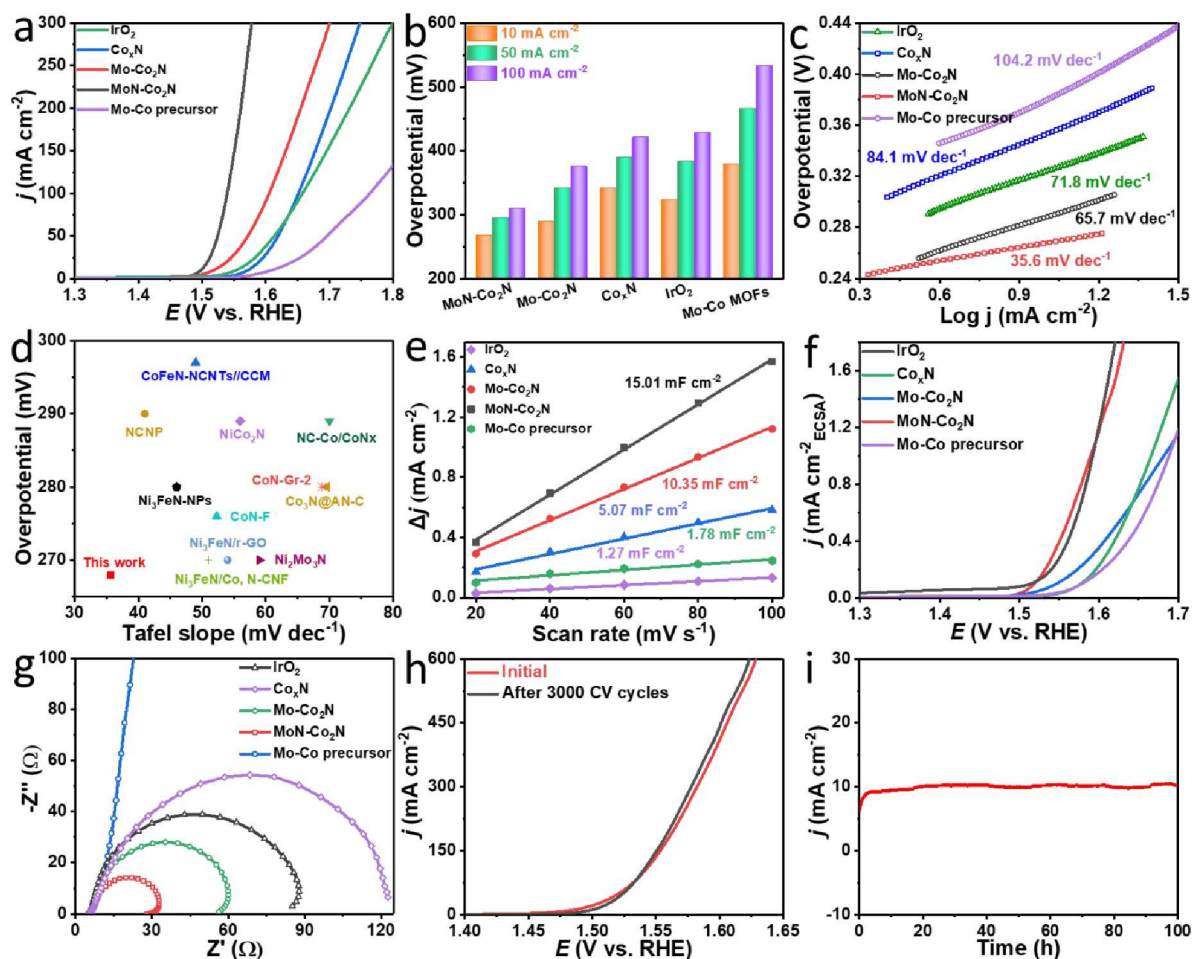
8

Figure 4. Electrocatalytic OER performance of the various catalysts. a) LSV curves. b) Overpotentials at 10, 50 and 100 mA cm^{-2}. c) Tafel plots. d) Comparison of overpotential at 10 mA cm^{-2} and Tafel slopes of MoN-Co$_2$N and other cobalt-based OER catalysts (Table S1). e) Capacitive current density measured at 1.17 V vs. RHE plotted as a function of scan rate. f) ECSA-normalized OER polarization curves. g) Nyquist plots. h) LSV curves before and after 3000 cycles. i) Chronoamperometry curves.

DFT calculations were used to obtain a deeper insight into the MoN-Co$_2$N heterointerface and to unveil the underlying reason for its enhanced OER electrocatalytic activity. The description of the model and the details of the calculation are provided in the support information. The partial density of states (DOS) of individual atoms on the surface of Co$_2$N and MoN-Co$_2$N (Figure 5a and S13) were used to study the electronic structure. The DOS value of MoN-Co$_2$N at the Fermi level was significantly larger than that of Co$_2$N, pointing to the availability of a larger density of free electrons for redox reactions in MoN-Co$_2$N.[46] Besides, the d-band center of Co$_2$N and MoN-Co$_2$N were −1.40 and −1.53 eV, respectively, i.e. the d-band center of MoN-Co$_2$N was farther away from the Fermi level compared with Co$_2$N.

Figures 5d and S14 display a scheme of the four-reaction steps involved in the OER. Surface Co and Mo metal atoms are assumed as the active adsorption sites of the reaction intermediates, i.e. *OH, *O, and *OOH. To determine the rate-determining step (RDS) and the theoretical overpotential, the Gibbs free energy of each of the OER intermediates was calculated. From these data, the O-O coupling process was determined as the RDS.[21] The calculated overpotential of MoN-Co$_2$N is 1.68 eV, far below the 3.02 eV of Co$_2$N (Figure 5b, c). Therefore, the metal nitride heterointerface enables a lower OER energy barrier and thus a much higher catalytic activity.[47] DOS data also point at a metallic character of the catalysts, with no gap of states at the Fermi level, which facilitates charge transport. Additional insights were obtained from the calculation of the d-band center (E$_d$, Figure 5a). According to the Sabatier principle, a moderate bonding of the reaction intermediates is necessary to maximize the electrocatalytic activity.[48] While high E$_d$ energy levels have empty antibonding states, thus a strong binding that is detrimental to the desorption of oxygen, [49, 50] the dual-phase nitride endows the surface with an appropriated E$_d$ energy level and balances the *O 2p level, thus maximizing the OER activity.
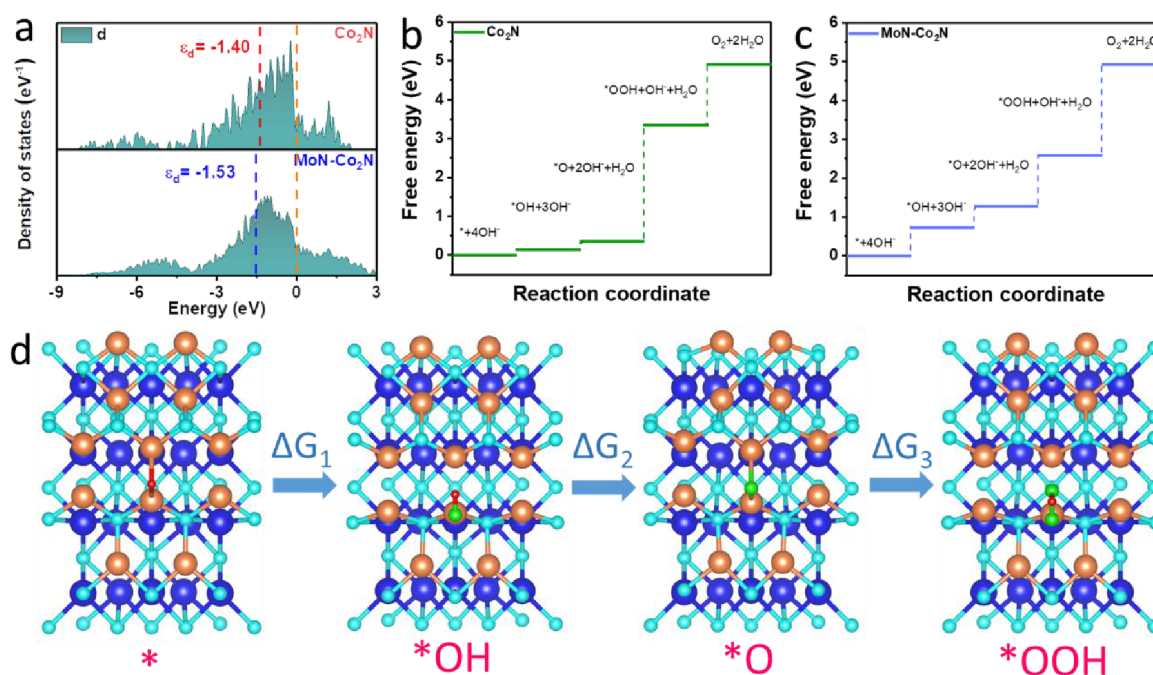

Figure 5 a) The d-band centers of Co 3d partial density of states, b, c) Gibbs free energy diagrams of OER intermediates of the for Co$_2$N and MoN-Co$_2$N and d) The evolutions of local structural configurations for illustrating OER process of MoN-Co$_2$N. (* represents the active site).

1
2
3
4
5
6
7
8
9
10
11
12
13
14
15
16
17
18
19
20
21
22
23
24
25
26
27
28
29
30
31

2.3. Hydrogen evolution reaction

The HER activities of the Co_xN, $Mo-Co_2N$, $MoN-Co_2N$ and Mo-Co precursor electrodes were compared with that of the reference Pt/C (Figure 6a). Among the TMNs, the $MoN-Co_2N$ electrocatalyst exhibited the lowest overpotential, 105 mV, to reach a current density of 10 mA cm^{-2}. This overpotential was slightly above that of Pt/C (87 mV), but it was lower than that of $Mo-Co_2N$ (144 mV), Co_xN (292 mV), and also Mo-Co precursor (474 mV), and it was competitive with state of the art HER noble-metal-free electrocatalysts (Table S3). As shown in Figure 6b, c, the Tafel slope of $MoN-Co_2N$ was 82.1 mV dec^{-1}, much smaller than those of $Mo-Co_2N$ (110.6 mV dec^{-1}), Co_xN (125.5 mV dec^{-1}) and Mo-Co precursor (143.2 mV dec^{-1}), and close to the Tafel Slope of Pt/C (69.1 mV dec^{-1}). These results suggest a Volmer-Heyrovsky HER mechanism for $Mo-Co_2N$, like Pt/C, where the reaction rate is determined by the electrodesorption step.[51] Figure 6d shows the Nyquist plots of the EIS data obtained from the different catalysts. Notice how the smallest diameter of the measured semicircle, indicating the charge transfer resistance (R_{ct}), was obtained with $MoN–Co_2N$ (R_{ct}=13.7 Ω) and Pt/C (R_{ct}=9.3 Ω) catalysts. As for HER, the long-term chronopotentiometric measurements (Figure 6e) also confirmed the electrochemical stability of the $MoN–Co_2N$ catalysts.

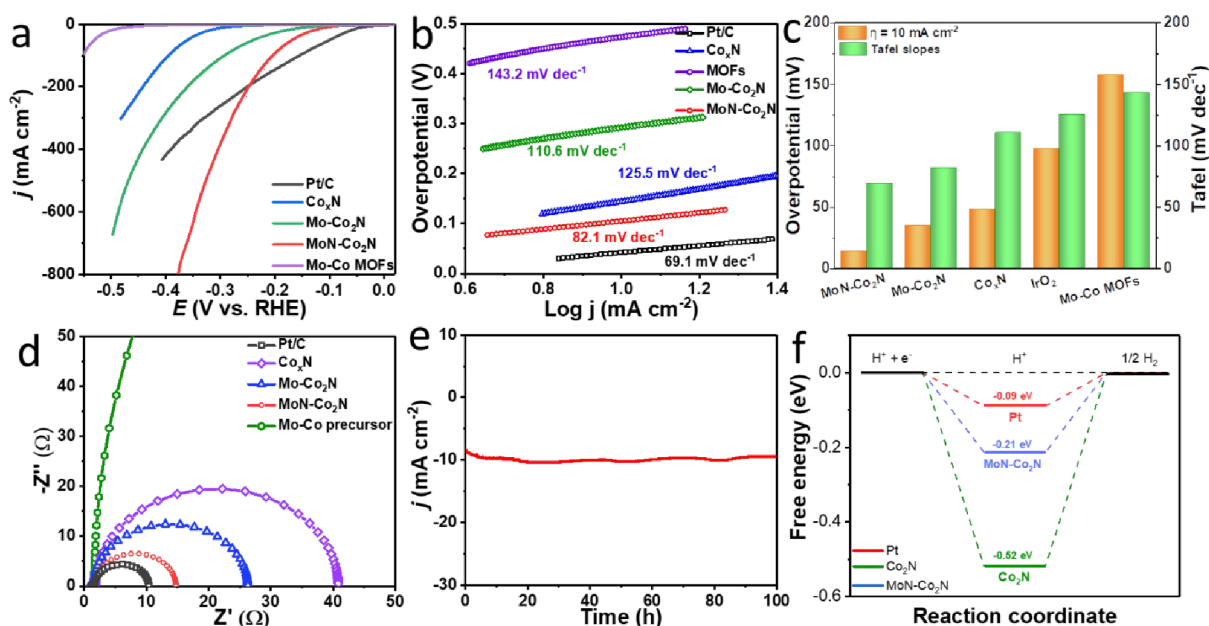**Figure 6.** HER performance of Pt/C, Co_xN, $Mo-Co_2N$, $MoN-Co_2N$, Mo-Co precursor catalysts; a) LSV curves, b) Tafel plots, c) the comparison of overpotentials at 10 mA cm^{-2} and Tafel slopes of different, d) Nyquist plots, e) chronoamperometry tests, f) Calculated free energy diagram of H* adsorption on the surface of Pt, Co_2N, $MoN-Co_2N$.

As noted above, DFT calculations showed that the DOS of MoN-Co$_2$N at the Fermi level was significantly larger than that of Co$_2$N, which involves a larger density of free electrons available for redox reactions.[46] DFT calculations also showed the d-band center of MoN-Co$_2$N to be farther away from the Fermi level compared with Co$_2$N. Being the d-band center a good descriptor of the metal-adsorbate bonding strength, the downshift of the d-band center also involves a weaker interaction between adsorbed H and MoN-Co$_2$N, thus faster desorption.[20, 22] This effect is reflected in the free energy of H adsorption (ΔG_{H*}). As shown in Figure 6f, the ΔG_{H*} of Co$_2$N was −0.52 eV, which was well above (in absolute value) that of MoN-Co$_2$N, −0.21 eV. The much lower absolute value of ΔG_{H*} is consistent with the downshift of the d-band center and explains the enhanced HER activity through the acceleration of the hydrogen desorption process.[42]

2.4. Seawater splitting

The main challenge for alkaline seawater splitting is the formation of electrode corroding hypochlorite on the anode side, where it competes with OER.[52] MoN-Co$_2$N is an excellent candidate electrocatalyst for seawater splitting as it requires an overpotential of only 309 mV to drive an OER current density of 100 mA cm^{-2} in 1 M KOH electrolyte, well below the 490 mV that activates the formation of hypochlorite. Besides, metal nitrides present good corrosion resistance, which is a fundamental catalyst requirement to be used for seawater splitting.[17, 53]

Owing to the excellent activity and stability of MoN-Co$_2$N, we tested it in an alkaline saline electrolyte (1 M KOH + 1 M NaCl aqueous electrolyte, simulating seawater) and in alkaline natural seawater (1 M KOH seawater) after filtering the formed hydroxides (see details in the SI, Figure S15). As displayed in Figure 7a,b, the OER and HER performance of the MoN-Co$_2$N catalyst in 1 M KOH seawater were below those obtained in 1 M KOH and 1 M KOH + 1 M NaCl water. The lower electrocatalytic activity in seawater is associated with the blocking/poisoning of the catalyst sites by the natural seawater impurities, e.g. ions, molecules, suspended particles, and microbes. Specifically, in 1 M KOH seawater electrolyte, the MoN-Co$_2$N electrocatalyst required OER overpotentials of 357 mV (100 mA cm^{-2}) and 432 mV (500 mA cm^{-2}) and HER overpotentials of 304 mV (100 mA cm^{-2}) and 451 mV (500 mA cm^{-2}). The overpotentials needed for MoN-Co$_2$N to drive current densities of 10, 100 and 500 mA cm^{-2} in 1 M KOH, 1 M KOH in NaCl water and 1 M KOH seawater electrolytes as an OER and an HER electrocatalyst are summarized in Figure 7c.

The overall water/seawater splitting performance was investigated using a two-electrode cell that

included the MoN-Co$_2$N electrocatalyst both at the anode and cathode (MoN-Co$_2$N ‖ MoN-Co$_2$N).

To drive 100 mA cm^{-2} of current density in a 1 M KOH electrolyte (Figure 7d), the MoN-Co$_2$N-based

cell required 1.63 V, well below the voltage required by the Pt/C ‖ IrO$_2$ -cell (1.66 V). Besides, for

overall seawater splitting, the MoN-Co$_2$N ‖ MoN-Co$_2$N cell required a voltage of 1.70 V to achieve

100 mA cm^{-2} in 1 M KOH seawater (Figure 7e, Table S4). In terms of durability, chronopotentiometry

analysis showed the MoN-Co$_2$N cell to be characterized by a sustained voltage at 100 mA cm^{-2} both

in alkaline water and alkaline seawater, with a minor raise of potential over 62 h of continuous

operation (Figure 7f). Additionally, Figure S16 displays the water splitting performance obtained

when adding no KOH to the seawater and Figure S17 displays data with and without ionic strength
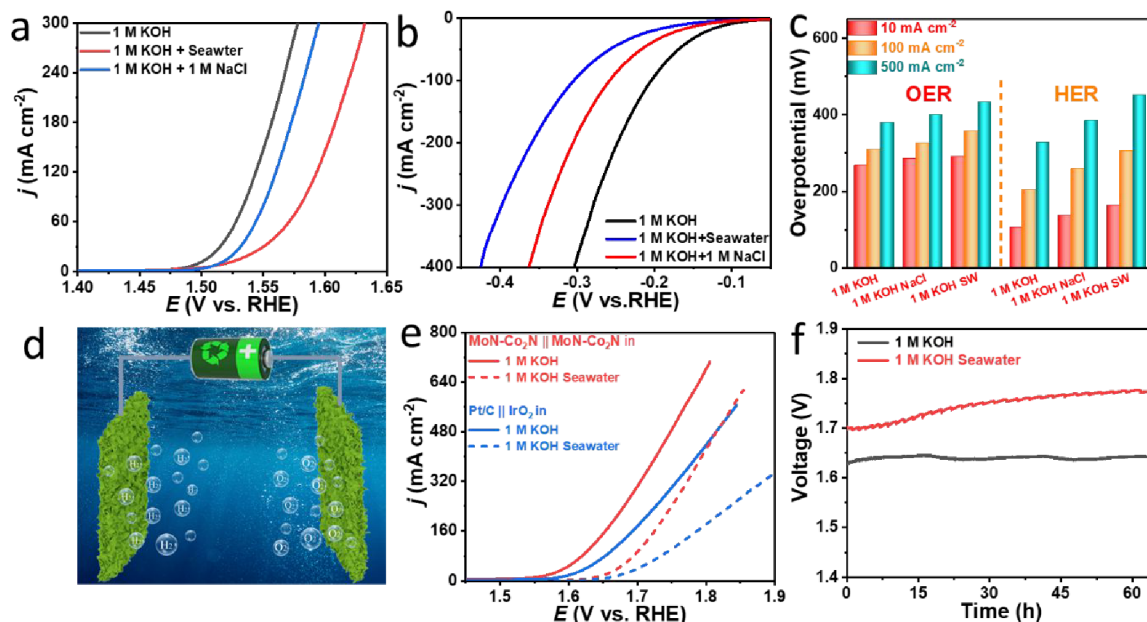
compensation (see details in the SI).

Figure 7. a-b) The LSV curves of the MoN-Co$_2$N/NF ‖ MoN-Co$_2$N/NF and Pt/C ‖ IrO$_2$ devices, c) Overpotentials required for the MoN-Co$_2$N electrocatalyst to achieve current densities of 10, 100 and 500 mA cm^{-2} for OER and HER in 1 m KOH, 1 M KOH in NaCl water, 1 M KOH seawater electrolytes. d) Schematic of the water-splitting device fabrication, e) Overall water/seawater splitting performance of MoN-Co$_2$N/NF ‖ MoN-Co$_2$N/NF and Pt/C ‖ IrO$_2$ pair in 1 M KOH and 1 M KOH seawater, f) Chronopotentiometry measurement at 100 mA cm^{-2}

Iodometric titration indicated the absence of any hypochlorite trace as shown by the colourless OER

solution shown in Figure S18a when compared with the pink colour of the reference solution. This

result confirmed the hampering of the chlorine evolution reaction in these conditions with no by-

product ClO$^-$ forming. To confirm the high Faradaic efficiency of the process, gas chromatography

was used to measure the amount of H$_2$ and O$_2$ gases produced by the MoN-Co$_2$N ‖ MoN-Co$_2$N cell.

13

The measured amount matched well the theoretical prediction (see SI for details), confirming a nearly 100% Faradaic efficiency (Figure S18b).

Finally, we examined the structural and chemical properties of the MoN-Co$_2$N catalyst after the long-term stability test in 1 M KOH + seawater electrolyte. High-resolution XPS data confirmed the surface of the particles to be completely oxidized (Figure S19). Besides, TEM and HAADF-STEM images of MoN-Co$_2$N after the long-term reaction showed the material to keep a porous NS structure, proving its high stability (Figure S20). Moreover, EELS elemental maps demonstrated the homogeneous distribution of the different metals, Mo and Co, within each NS to be maintained and the NS to still contain large amounts of N, although the surface of the catalyst appeared to be fully oxidized (Figure S21).

3. Conclusion

In summary, MoN-Co$_2$N NSs were synthesized using ZIF-67 as a self-sacrificial template through proton etching, ion exchange, and metal nitridation processes. The porous NS structure enables an effective proper electrolyte diffusion and accelerates the release of bubbles, which translates into outstanding catalytic activities and stabilities even at high current density. The prepared MoN-Co$_2$N electrocatalysts possess excellent OER and HER catalytic activity, requiring an overpotential of 267 and 105 mV to drive OER and HER at 10 mA cm^{-2} current density in 1.0 M KOH electrolyte, respectively. As for overall water/seawater splitting, a system based on an MoN-Co$_2$N bifunctional electrocatalyst only required voltages of 1.63 and 1.70 V to reach a current density of 100 mA cm^{-2} in 1 M KOH freshwater and 1 M KOH natural seawater, respectively. These overpotentials are significantly lower than those required by the benchmark IrO$_2$-Pt/C pair. DFT calculations revealed the MoN-Co$_2$N to be characterized by a proper d-band center that provided low OER and HER energy barriers and a balanced intermediates adsorption strength. Overall, this work presented a novel nitride electrocatalyst for the cost-effective and stable production of hydrogen production from seawater.

Acknowledgements

References

1. Liu, Y.; Xiao, C.; Huang, P.; Cheng, M.; Xie, Y., Regulating the Charge and Spin Ordering of Two-Dimensional Ultrathin Solids for Electrocatalytic Water Splitting. *Chem* **2018,** *4* (6), 1263-1283.

2. Tong, W.; Forster, M.; Dionigi, F.; Dresp, S.; Sadeghi Erami, R.; Strasser, P.; Cowan, A. J.; Farràs, P., Electrolysis of low-grade and saline surface water. *Nat. Energy* **2020,** *5* (5), 367-377.

3. Liu, Y.; Xiao, C.; Huang, P.; Cheng, M.; Xie, Y., Regulating the Charge and Spin Ordering of Two-Dimensional Ultrathin Solids for Electrocatalytic Water Splitting. *Chem* **2018,** *4* (6), 1263-1283.

4. Tian, X.; Zhao, P.; Sheng, W., Hydrogen Evolution and Oxidation: Mechanistic Studies and Material Advances. *Adv Mater* **2019,** *31* (31), e1808066.

5. Sun, H.; Xu, X.; Song, Y.; Zhou, W.; Shao, Z., Designing High-Valence Metal Sites for Electrochemical Water Splitting. *Adv. Funct. Mater.* **2021,** *31* (16).

6. Ifkovits, Z. P.; Evans, J. M.; Meier, M. C.; Papadantonakis, K. M.; Lewis, N. S., Decoupled electrochemical water-splitting systems: a review and perspective. *Energy Environ. Sci.* **2021,** *14* (9), 4740-4759.

7. Huang, Y.; Hu, L.; Liu, R.; Hu, Y.; Xiong, T.; Qiu, W.; Balogun, M. S.; Pan, A.; Tong, Y., Nitrogen treatment generates tunable nanohybridization of Ni_5P_4 nanosheets with nickel hydr(oxy)oxides for efficient hydrogen production in alkaline, seawater and acidic media. *Appl. Catal. B.* **2019,** *251*, 181-194.

8. Zhao, Y.; Jin, B.; Zheng, Y.; Jin, H.; Jiao, Y.; Qiao, S. Z., Charge State Manipulation of Cobalt Selenide Catalyst for Overall Seawater Electrolysis. *Adv. Energy Mater.* **2018,** *8* (29).

9. Bigiani, L.; Barreca, D.; Gasparotto, A.; Andreu, T.; Verbeeck, J.; Sada, C.; Modin, E.; Lebedev, O. I.; Morante, J. R.; Maccato, C., Selective anodes for seawater splitting via functionalization of manganese oxides by a plasma-assisted process. *Appl. Catal. B.* **2021,** *284*.

10. Dresp, S.; Dionigi, F.; Klingenhof, M.; Strasser, P., Direct Electrolytic Splitting of Seawater: Opportunities and Challenges. *ACS Energy Letters* **2019,** *4* (4), 933-942.

11. Yuan, W.; Cui, Z.; Zhu, S.; Li, Z.; Wu, S.; Liang, Y., Structure engineering of electrodeposited NiMo films for highly efficient and durable seawater splitting. *Electrochim. Acta* **2021,** *365*.

12. Ros, C.; Murcia-Lopez, S.; Garcia, X.; Rosado, M.; Arbiol, J.; Llorca, J.; Morante, J. R., Facing Seawater Splitting Challenges by Regeneration with Ni-Mo-Fe Bifunctional Electrocatalyst for Hydrogen and Oxygen Evolution. *ChemSusChem* **2021,** *14* (14), 2872-2881.

13. Sun, F.; Qin, J.; Wang, Z.; Yu, M.; Wu, X.; Sun, X.; Qiu, J., Energy-saving hydrogen production by chlorine-free hybrid seawater splitting coupling hydrazine degradation. *Nat. Commun* **2021,** *12* (1), 4182.

14. Wang, C.; Shang, H.; Jin, L.; Xu, H.; Du, Y., Advances in hydrogen production from electrocatalytic seawater splitting. *Nanoscale* **2021,** *13* (17), 7897-7912.

15. Dresp, S.; Dionigi, F.; Loos, S.; Ferreira de Araujo, J.; Spöri, C.; Gliech, M.; Dau, H.; Strasser, P., Direct Electrolytic Splitting of Seawater: Activity, Selectivity, Degradation, and Recovery Studied from the Molecular Catalyst Structure to the Electrolyzer Cell Level. *Adv. Energy Mater.* **2018,** *8* (22).

16. Dresp, S.; Ngo Thanh, T.; Klingenhof, M.; Brückner, S.; Hauke, P.; Strasser, P., Efficient direct seawater electrolysers

using selective alkaline NiFe-LDH as OER catalyst in asymmetric electrolyte feeds. *Energy Environ. Sci.* **2020,** *13* (6), 1725-1729.

17.　Jin, H.; Liu, X.; Vasileff, A.; Jiao, Y.; Zhao, Y.; Zheng, Y.; Qiao, S. Z., Single-Crystal Nitrogen-Rich Two-Dimensional Mo5N6 Nanosheets for Efficient and Stable Seawater Splitting. *ACS Nano* **2018,** *12* (12), 12761-12769.

18.　Yu, L.; Zhu, Q.; Song, S.; McElhenny, B.; Wang, D.; Wu, C.; Qin, Z.; Bao, J.; Yu, Y.; Chen, S.; Ren, Z., Non-noble metal-nitride based electrocatalysts for high-performance alkaline seawater electrolysis. *Nat Commun* **2019,** *10* (1), 5106.

19.　Han, N.; Liu, P.; Jiang, J.; Ai, L.; Shao, Z.; Liu, S., Recent advances in nanostructured metal nitrides for water splitting. *J. Mater. Chem. A* . **2018,** *6* (41), 19912-19933.

20.　Chen, Z.; Song, Y.; Cai, J.; Zheng, X.; Han, D.; Wu, Y.; Zang, Y.; Niu, S.; Liu, Y.; Zhu, J.; Liu, X.; Wang, G., Tailoring the d-Band Centers Enables Co4 N Nanosheets To Be Highly Active for Hydrogen Evolution Catalysis. *Angew. Chem. Int. Ed.* **2018,** *57* (18), 5076-5080.

21.　Chen, Q.; Gong, N.; Zhu, T.; Yang, C.; Peng, W.; Li, Y.; Zhang, F.; Fan, X., Surface Phase Engineering Modulated Iron-Nickel Nitrides/Alloy Nanospheres with Tailored d-Band Center for Efficient Oxygen Evolution Reaction. *Small* **2021**, 2105696.

22.　Hu, Y.; Huang, D.; Zhang, J.; Huang, Y.; Balogun, M. S. J. T.; Tong, Y., Dual Doping Induced Interfacial Engineering of Fe2N/Fe3N Hybrids with Favorable d-Band towards Efficient Overall Water Splitting. *ChemCatChem* **2019,** *11* (24), 6051-6060.

23.　Jadhav, H. S.; Bandal, H. A.; Ramakrishna, S.; Kim, H., Critical Review, Recent Updates on Zeolitic Imidazolate Framework-67 (ZIF-67) and Its Derivatives for Electrochemical Water Splitting. *Adv Mater* **2021**, e2107072.

24.　Zhang, B.; Zheng, Y.; Ma, T.; Yang, C.; Peng, Y.; Zhou, Z.; Zhou, M.; Li, S.; Wang, Y.; Cheng, C., Designing MOF Nanoarchitectures for Electrochemical Water Splitting. *Adv Mater* **2021,** *33* (17), e2006042.

25.　Guo, C.; Liu, X.; Gao, L.; Ma, X.; Zhao, M.; Zhou, J.; Kuang, X.; Deng, W.; Sun, X.; Wei, Q., Oxygen defect engineering in cobalt iron oxide nanosheets for promoted overall water splitting. *J. Mater. Chem. A* **2019,** *7* (38), 21704-21710.

26. Xu, H.; Fei, B.; Cai, G.; Ha, Y.; Liu, J.; Jia, H.; Zhang, J.; Liu, M.; Wu, R., Boronization-Induced Ultrathin 2D Nanosheets with Abundant Crystalline–Amorphous Phase Boundary Supported on Nickel Foam toward Efficient Water Splitting. *Adv. Energy Mater.* **2019,** *10* (3).

27. Zhang, Y.; Shao, Q.; Long, S.; Huang, X., Cobalt-molybdenum nanosheet arrays as highly efficient and stable earth-abundant electrocatalysts for overall water splitting. *Nano Energy* **2018,** *45*, 448-455.

28. Cheng, W.; Wu, Z. P.; Luan, D.; Zang, S. Q.; Lou, X. W., Synergetic Cobalt-Copper-Based Bimetal–Organic Framework Nanoboxes toward Efficient Electrochemical Oxygen Evolution. *Angew. Chem. Int. Ed.* **2021,** *60* (50), 26397-26402.

29. Huang, Y.; Zhang, S. L.; Lu, X. F.; Wu, Z. P.; Luan, D.; Lou, X. W. D., Trimetallic Spinel NiCo$_{2-x}$Fe$_x$O$_4$ Nanoboxes for Highly Efficient Electrocatalytic Oxygen Evolution. *Angew. Chem. Int. Ed.* **2021,** *60* (21), 11841-11846.

30. Wang, X.; Xing, C.; Liang, Z.; Guardia, P.; Han, X.; Zuo, Y.; Llorca, J.; Arbiol, J.; Li, J.; Cabot, A., Activating the lattice oxygen oxidation mechanism in amorphous molybdenum cobalt oxide nanosheets for water oxidation. *J. Mater. Chem. A* **2022**.

31. Wang, W.; Yan, H.; Anand, U.; Mirsaidov, U., Visualizing the Conversion of Metal-Organic Framework Nanoparticles into Hollow Layered Double Hydroxide Nanocages. *J. Am. Chem. Soc.* **2021,** *143* (4), 1854-1862.

32. Guo, H.; Wu, A.; Xie, Y.; Yan, H.; Wang, D.; Wang, L.; Tian, C., 2D porous molybdenum nitride/cobalt nitride heterojunction nanosheets with interfacial electron redistribution for effective electrocatalytic overall water splitting. *J. Mater. Chem. A* **2021,** *9* (13), 8620-8629.

33. Lan, K.; Wang, X.; Yang, H.; Iqbal, K.; Zhu, Y.; Jiang, P.; Tang, Y.; Yang, Y.; Gao, W.; Li, R., Ultrafine MoP Nanoparticles Well Embedded in Carbon Nanosheets as Electrocatalyst with High Active Site Density for Hydrogen

Evolution. *ChemElectroChem* **2018**, *5* (16), 2256-2262.

34. Ouyang, T.; Wang, X. T.; Mai, X. Q.; Chen, A. N.; Tang, Z. Y.; Liu, Z. Q., Coupling Magnetic Single-Crystal $Co_2Mo_3O_8$ with Ultrathin Nitrogen-Rich Carbon Layer for Oxygen Evolution Reaction. *A Angew. Chem. Int. Ed.* **2020,** *59* (29), 11948-11957.

35. Yu, L.; Wu, L.; McElhenny, B.; Song, S.; Luo, D.; Zhang, F.; Yu, Y.; Chen, S.; Ren, Z., Ultrafast room-temperature synthesis of porous S-doped Ni/Fe (oxy)hydroxide electrodes for oxygen evolution catalysis in seawater splitting. *Energy Environ. Sci.*, **2020**, 13 (10), 3439-3446..

36. Chen, Z.; Ha, Y.; Liu, Y.; Wang, H.; Yang, H.; Xu, H.; Li, Y.; Wu, R., In Situ Formation of Cobalt Nitrides/Graphitic Carbon Composites as Efficient Bifunctional Electrocatalysts for Overall Water Splitting. *ACS Appl Mater Interfaces* **2018,** *10* (8), 7134-7144.

37. Choi, H. W.; Jeong, D. I.; Woo, S.; Kwon, S. B.; Wu, S.; Kim, J. H.; Yang, W. S.; Kang, B. K.; Lim, B.; Yoon, D. H., Morphology adjustable CoxN with 3D mesoporous structure and amorphous N-doped carbon for overall water splitting. *Appl. Surf. Sci.* **2020,** *529.*

38. Shu, X.; Chen, S.; Chen, S.; Pan, W.; Zhang, J., Cobalt nitride embedded holey N-doped graphene as advanced bifunctional electrocatalysts for Zn-Air batteries and overall water splitting. *Carbon* **2020,** *157,* 234-243.

39. Yao, R. Q.; Shi, H.; Wan, W. B.; Wen, Z.; Lang, X. Y.; Jiang, Q., Flexible Co-Mo-N/Au Electrodes with a Hierarchical Nanoporous Architecture as Highly Efficient Electrocatalysts for Oxygen Evolution Reaction. *Adv. Mater.,* **2020,** *32* (10), e1907214.

40. Guan, H.; Yi, W.; Li, T.; Li, Y.; Li, J.; Bai, H.; Xi, G., Low temperature synthesis of plasmonic molybdenum nitride nanosheets for surface enhanced Raman scattering. *Nat. Commun.,* **2020,** *11* (1), 1-9.

41. Zou, H.; Li, G.; Duan, L.; Kou, Z.; Wang, J., In situ coupled amorphous cobalt nitride with nitrogen-doped graphene aerogel as a trifunctional electrocatalyst towards Zn-air battery deriven full water splitting. *Appl. Catal. B.,* **2019,** *259.*

42. Ma, H.; Chen, Z.; Wang, Z.; Singh, C. V.; Jiang, Q., Interface Engineering of Co/CoMoN/NF Heterostructures for High-Performance Electrochemical Overall Water Splitting. *Adv. Sci.,* **2022**, e2105313.

43. Yoon, K. R.; Hwang, C. K.; Kim, S. H.; Jung, J. W.; Chae, J. E.; Kim, J.; Lee, K. A.; Lim, A.; Cho, S. H.; Singh, J. P.; Kim, J. M.; Shin, K.; Moon, B. M.; Park, H. S.; Kim, H. J.; Chae, K. H.; Ham, H. C.; Kim, I. D.; Kim, J. Y., Hierarchically Assembled Cobalt Oxynitride Nanorods and N-Doped Carbon Nanofibers for Efficient Bifunctional Oxygen Electrocatalysis with Exceptional Regenerative Efficiency. *ACS Nano* **2021**.

44. Lu, Y.; Li, Z.; Xu, Y.; Tang, L.; Xu, S.; Li, D.; Zhu, J.; Jiang, D., Bimetallic Co-Mo nitride nanosheet arrays as high-performance bifunctional electrocatalysts for overall water splitting. *Chem. Eng. J.* **2021,** *411.*

45. Yao, N.; Meng, R.; Su, J.; Fan, Z.; Zhao, P.; Luo, W., Dual-phase engineering of MoN/Co_4N with tailored electronic structure for enhanced hydrogen evolution. *Chem. Eng. J.* **2021,** *421.*

46. Wu, L.; Yu, L.; Zhang, F.; McElhenny, B.; Luo, D.; Karim, A.; Chen, S.; Ren, Z., Heterogeneous Bimetallic Phosphide Ni_2P-Fe_2P as an Efficient Bifunctional Catalyst for Water/Seawater Splitting. *Adv. Funct. Mater.* **2020,** *31* (1).

47. Wang, Z.; Lin, Z.; Deng, J.; Shen, S.; Meng, F.; Zhang, J.; Zhang, Q.; Zhong, W.; Gu, L., Elevating the d-Band Center of Six-Coordinated Octahedrons in Co_9S_8 through Fe-Incorporated Topochemical Deintercalation. *Adv. Energy Mater.* **2021,** *11* (5), 2003023.

48. Jiao, S.; Fu, X.; Huang, H., Descriptors for the Evaluation of Electrocatalytic Reactions: d-Band Theory and Beyond. *Adv. Funct. Mater.,* **2021**, 2107651.

49. Wang, Z.; Shen, S.; Lin, Z.; Tao, W.; Zhang, Q.; Meng, F.; Gu, L.; Zhong, W., Regulating the Local Spin State and Band Structure in Ni_3S_2 Nanosheet for Improved Oxygen Evolution Activity. *Adv. Funct. Mater.,* **2022**, 2112832.

50. Tang, Y.; Shen, K.; Zheng, J.; He, B.; Chen, J.; Lu, J.; Ge, W.; Shen, L.; Yang, P.; Deng, S., d-Band center modulating of CoO_x/Co_9S_8 by oxygen vacancies for fast-kinetics pathway of water oxidation. *Chem. Eng. J.* **2022,** *427.*

51. Jin, J.; Yin, J.; Liu, H.; Huang, B.; Hu, Y.; Zhang, H.; Sun, M.; Peng, Y.; Xi, P.; Yan, C. H., Atomic Sulfur Filling

Oxygen Vacancies Optimizes H Absorption and Boosts the Hydrogen Evolution Reaction in Alkaline Media. *Angew. Chem. Int. Ed.* **2021,** *60* (25), 14117-14123.

52. Wang, X. H.; Ling, Y.; Wu, B.; Li, B. L.; Li, X. L.; Lei, J. L.; Li, N. B.; Luo, H. Q., Doping modification, defects construction, and surface engineering: Design of cost-effective high-performance electrocatalysts and their application in alkaline seawater splitting. *Nano Energy* **2021,** *87*.

53. Zhao, Y.; Jin, B.; Vasileff, A.; Jiao, Y.; Qiao, S.-Z., Interfacial nickel nitride/sulfide as a bifunctional electrode for highly efficient overall water/seawater electrolysis. *J. Mater. Chem. A* **2019,** *7* (14), 8117-8121.